Phys Chem Minerals (1989) 16:517–523

PHYSICS AND CHEMISTRY
OF MINERALS

The Structure and Microstructure of α-Cristobalite and Its Relationship to β-Cristobalite

R.L. Withers, J.G. Thompson, and T.R. Welberry
Research School of Chemistry, Australian National University, GPO Box 4, Canberra ACT 2601, Australia

Abstract. Recent *transmission electron microscopy* (TEM) electron diffraction investigation of β-cristobalite has revealed a strong characteristic diffuse intensity distribution. In this work a similar, but less intense, diffuse scattering is reported for synthetic α-cristobalite. This material also displays both tetragonal twinning and characteristic striations correspond to planar boundaries which may exist on any $\{1, 0, l\}_{\text{tetragonal}}$ plane.

Introduction

Structures based on networks of corner-connected tetrahedra of anions coordinating a central cation are among the more important in crystal chemistry. This paper is concerned with one of the simplest of such networks, and the structures derived from it. The starting point is the *C*9 structure originally proposed (Wyckoff 1925) for β-, or high-, cristobalite. It belongs to space group $Fd\bar{3}m$: BX_2, with B in 8(a) and X in 16(c). Two projections are shown in Figure 1. β-cristobalite is the stable polymorph of SiO_2 between 1625° C and 1470° C, but exists in a metastable form down to about 275° C, when it undergoes a rapid and reversible transition to (metastable) α- (low-) cristobalite.

Recently we (Hua et al. 1988) reported the existence of a very strong and characteristic diffuse intensity distribution in β-cristobalite. This diffuse intensity distribution took

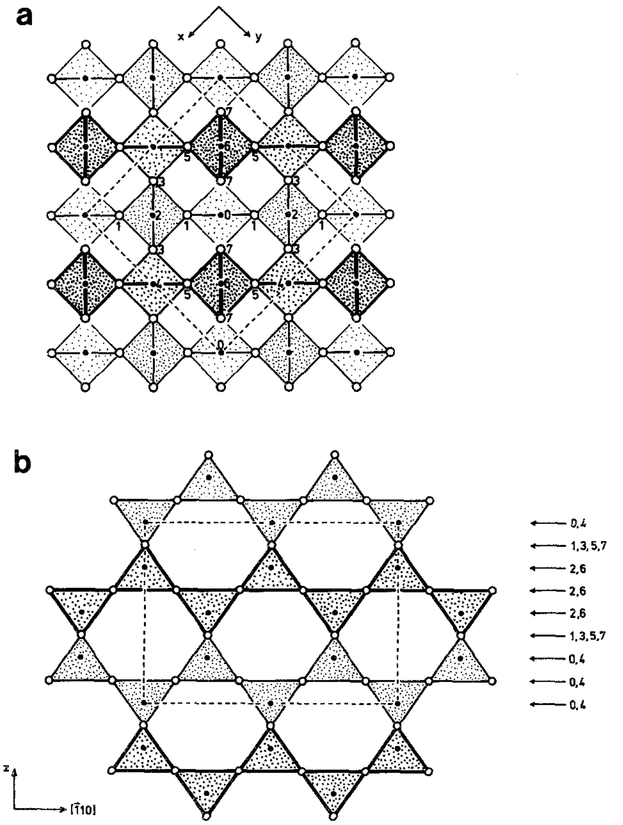

Fig. 1 a, b. Two projections of the *C*9 structure, BX_2 : (**a**) on (001), and (**b**) on (110) of the cubic, $Fd\bar{3}m$, unit cell (from O'Keeffe and Hyde 1976). *Small filled circles* are B atoms, *large open circles* are X atoms. Heights are in multiples of *c*/8 or *a* [110]/8

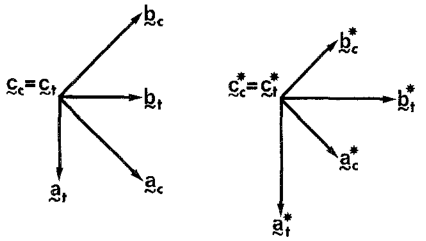

Fig. 2. The real and reciprocal space relationships between the tetragonal unit cell (subscript t) of the low-cristobalite structure ($P4_12_12$ or $P4_32_12$) and the cubic unit cell (subscript c) of the high-cristobalite structure ($Fd\bar{3}m$)

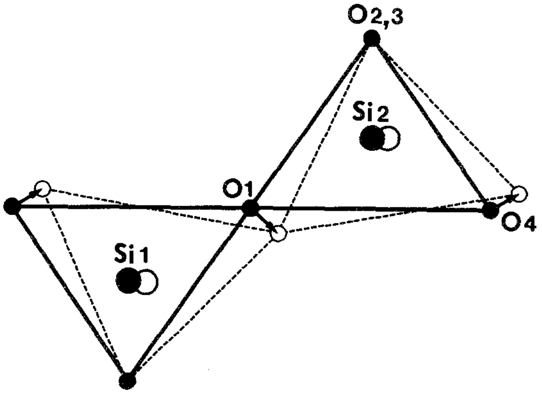

Fig. 3. Diagram showing the chosen displacement eigenvectors (*arrows*) associated with an R_{14} irreducible representation corresponding to coupled rotations of corner-connected tetrahedra along a <110> direction. In this projection, the same as in Figure 1b, O2 and O3 define one tetrahedral edge and project onto each other

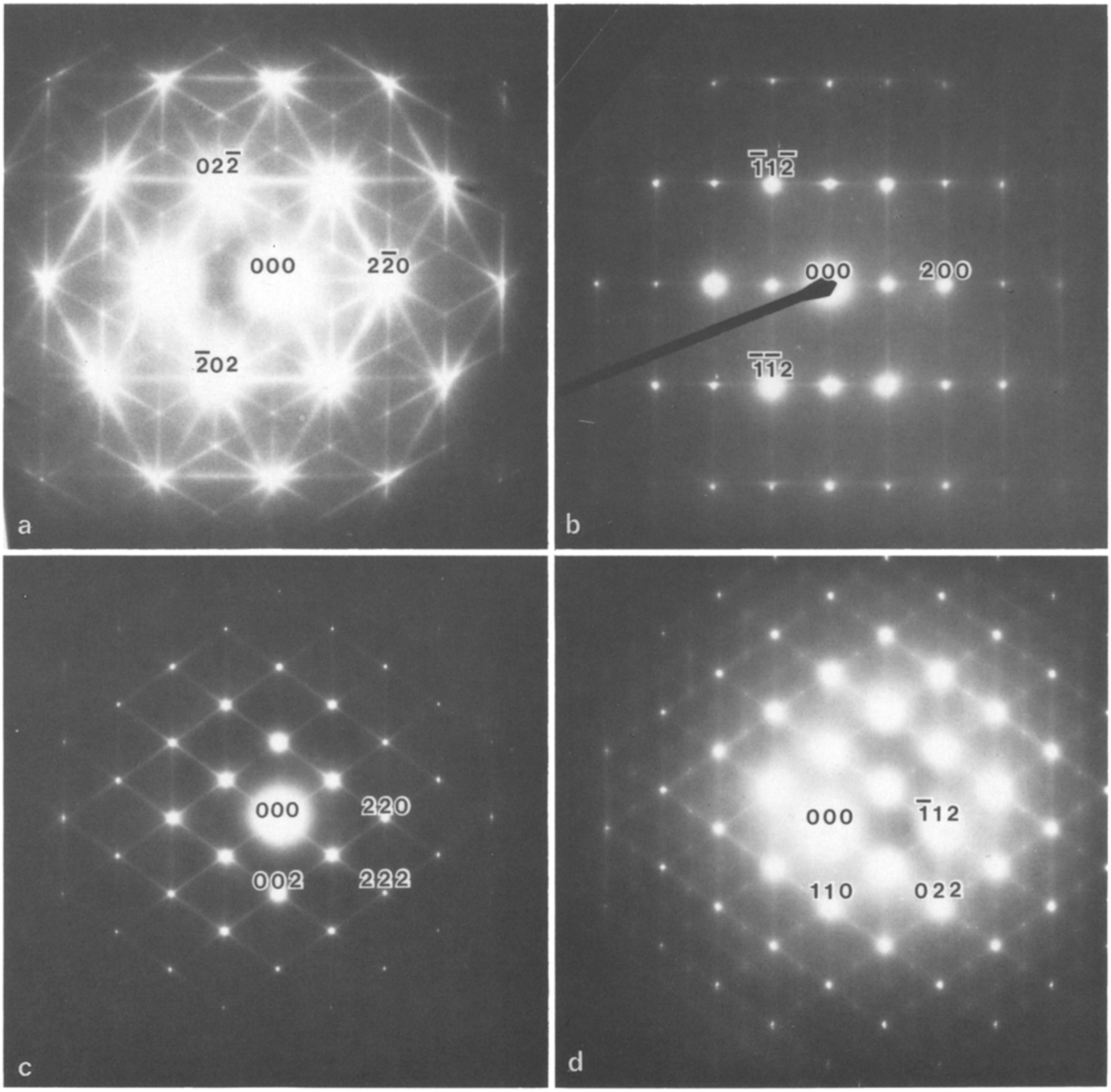

Fig. 4a–h. Various major zone axes SADP's of low-cristobalite, (**b**) $[021]_t$, (**d**) $[1\bar{1}1]_t$, (**f**) $[02\bar{2}]_t$, (**h**) $[001]_t$, juxtaposed to corresponding zone axes SADP's of high-cristobalite, (**a**) $[111]_c$, (**c**) $[1\bar{1}0]_c$, (**e**) $[11\bar{2}]_c$, (**g**) $[001]_c$. While of diminished intensity the diffuse distribution in low-cristobalite is closely related to that in high-cristobalite

the form of sheets normal to each of the six <110> directions, and was interpreted in terms of low-lying relatively dispersionless branches of the phonon dispersion curve diagrams. These branches correspond to motions of the structure involving coupled rotations of columns of corner-connected tetrahedra parallel to the <110> directions, the motions in neighbouring rows being virtually uncoupled.

This paper investigates the characteristic microstructure of α-cristobalite and its relationship to β-cristobalite.

Experimental

The specimen used in this investigation has been fully described in our previous work on β-cristobalite (Hua et al. 1988). Its $\alpha-\beta$ phase transition occurred at 538(5)K upon heating and at 513(10)K upon cooling. Mechanically crushed specimens were examined in a JEOL 100CX electron microscope using an EM-SHTH2 double-tilt heating holder.

While our synthetic cristobalite appeared more resistant to electron beam damage than naturally occurring specimens, a low beam intensity was still necessary to minimise electron beam damage and this precluded conventional high-resolution TEM investigation.

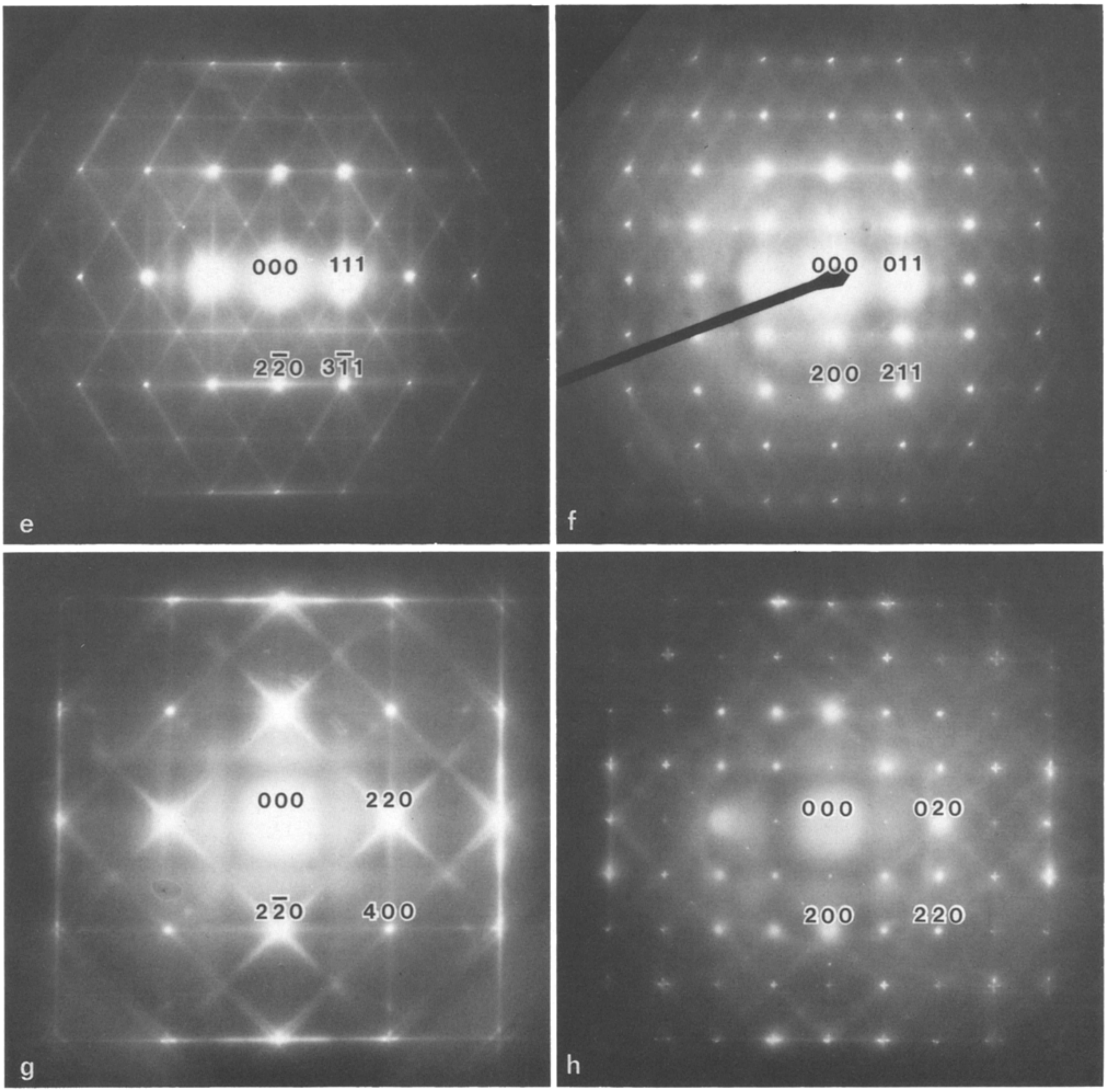

Relationship between *C*9, *β*- and *α*-cristobalite

The tetragonal unit cell of the low-cristobalite structure ($P4_12_12$ or $P4_32_12$, with $a_t = b_t \simeq 4.98$ Å, $c_t \simeq 6.95$ Å) is readily related to the cubic unit cell of high-cristobalite ($Fd\bar{3}m$, with a $\simeq 7.16$ Å). The relationship is close, as can be seen by constructing an appropriately chosen, enlarged *C*-centred tetragonal cell (with $a = b \simeq \sqrt{2} \times 4.98$ Å $= 7.04$ Å, $c \simeq 6.95$ Å), see Figure 2. The relationship between these two cells is spelled out in detail in Section 5.5 of the International Tables for Crystallography Vol A (1983) and need not be repeated here. Suffice it to say that reflections indexed as $(h, k, l)_t^*$ with respect to the *P* cell become $(h+k, -h+k, l)_c^*$ reflections when indexed with respect to the *C* cell (the subscripts *t* and *c* refer to the low- and high-cells). Apart from the small change in cell dimensions, the major difference between this *C*-centred cell and the $Fd\bar{3}m$, high-cristobalite cell is the lowering in Bravais lattice symmetry from *F* to *C*. Such a Bravais lattice symmetry lowering can, at least formally, be understood in terms of the condensation of a $\mathbf{q} = \mathbf{c}^*$ displacive modulation of the 'average' high-cristobalite structure, i.e., *C*9. The condensation of such a modulation would clearly destroy the $1/2(\mathbf{a}+\mathbf{c})$ and $1/2(\mathbf{b}+\mathbf{c})$ Bravais lattice translation symmetry operations but not the (*C*-centreing) $1/2(\mathbf{a}+\mathbf{b})$ translation symmetry operation.

Thus $1/2(\mathbf{a}+\mathbf{c})$ and $1/2(\mathbf{b}+\mathbf{c})$ displacement faults in low-cristobalite are possible. In turn, the cubic $Fd\bar{3}m$ parent symmetry implies that low-cristobalite should exhibit three tetragonal twin variants, corresponding to the condensation of $\mathbf{q} = \mathbf{a}^*$, $\mathbf{b}^*$ or $\mathbf{c}^*$ displacive modulations.

The strong intensity of the characteristic diffuse distribution present in high-cristobalite, however, makes it clear that one cannot really talk about a well-defined, parent

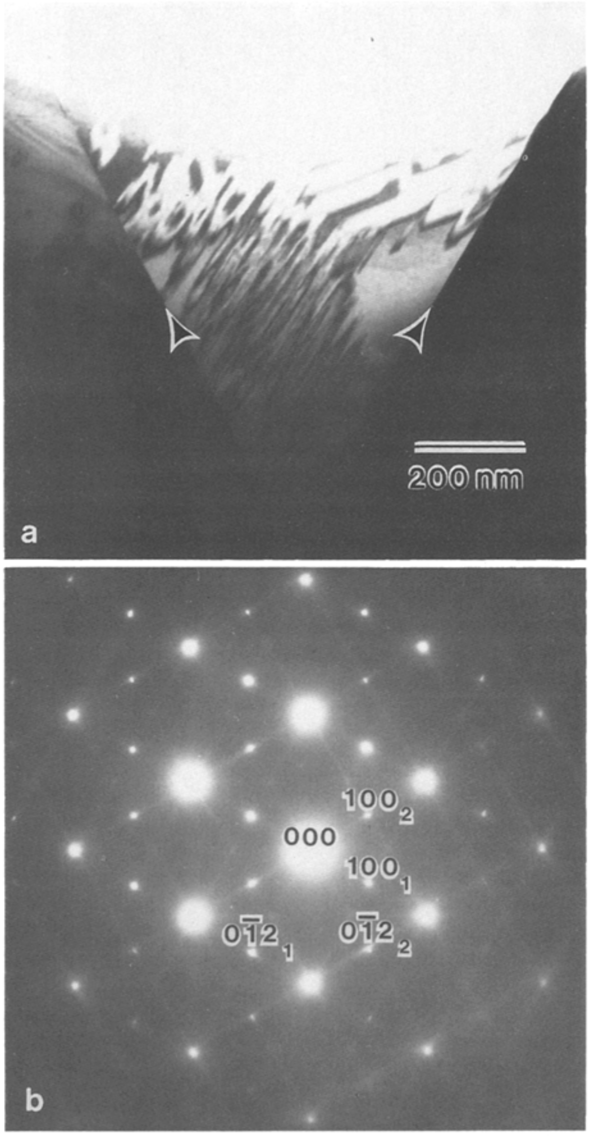

Fig. 5a, b. A low-magnification TEM bright-field image (**a**) of a crystal containing widely spaced twin boundaries separating two tetragonal variants along with the corresponding SADP (**b**). The Composition planes (*solid arrows*) are $\{112\}_t$ or $\{200\}_t \equiv \{101\}_c$

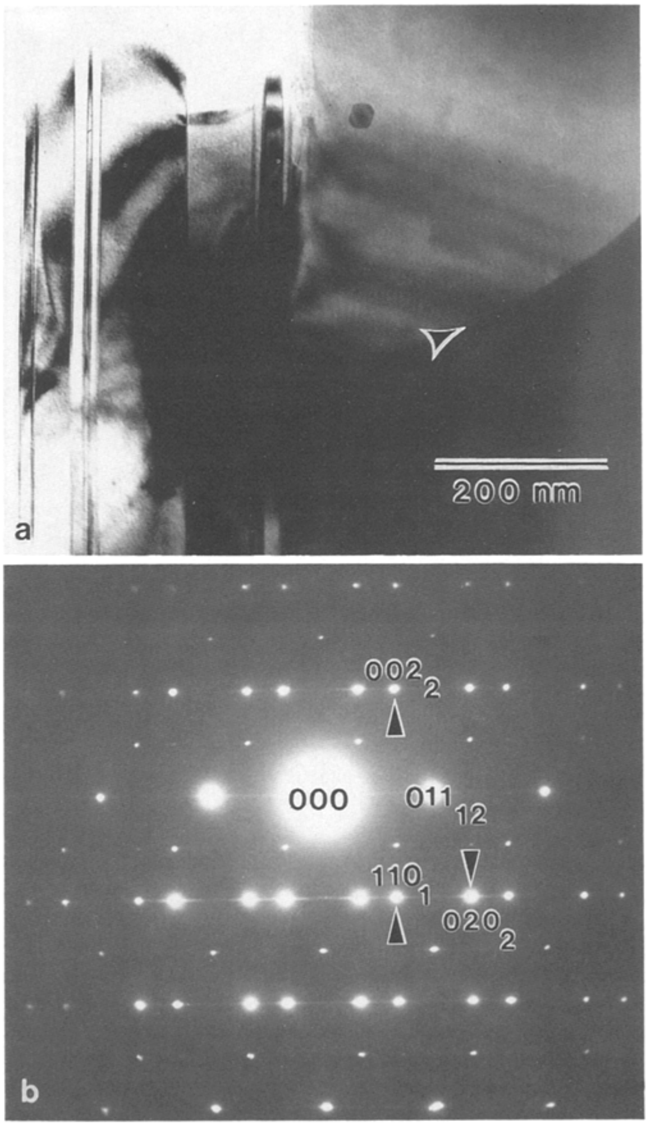

Fig. 6a, b. Low-magnification TEM bright-field image (**a**) and corresponding SADP (**b**) of a crystal containing tetragonal twin variants separated by a curved composition plane (*solid arrow*), as well as finer scale twinning with composition plane $\{011\}_t \equiv \{111\}_c$

high-cristobalite structure. Nevertheless, it is instructive to consider the displacement eigenvectors associated with a $\mathbf{q}=\mathbf{c}^*$ modulation of the $C9$ average structure. According to Bradley and Cracknell 1972 (pp 240 and 383), there exist four doubly degenerate irreducible representations associated with such modulation wave-vectors and labelled R_{10}, R_{11}, R_{13} and R_{14} respectively. It is not difficult to show that the doubly degenerate displacement eigenvectors (labelled e_A and e_B) associated with an R_{14} irreducible representation can be chosen so as to correspond to coupled rotations of rows of corner-connected tetrahedra parallel to the [110] and $[1\bar{1}0]$ directions respectively (see Fig. 3). Just such coupled motion along $<110>$ directions is responsible for the characteristic diffuse intensity distribution. Because e_A and e_B are doubly degenerate, it is of course possible to construct orthogonal linear combinations thereof. The choice (e_A+e_B) and (e_A-e_B) can be shown to give to the $P4_12_12$ and $P4_32_12$ enantiomorphs of low-cristobalite respectively. Summarizing then, one could anticipate a rather complex microstructure within low-cristobalite. Possible structural defects include twin boundaries between tetragonal twin variants, displacement faults within one tetragonal variant and enantiomorphic twinning within one tetragonal variant.

Results

1. Diffuse Intensity Distributions

Figure 4 shows room temperature $[021]_t$, $[1\bar{1}1]_t$, $[02\bar{2}]_t$ and $[001]_t$ zone axis diffraction patterns from low-cristobalite juxtaposed to the corresponding ~600 K zone axis diffraction patterns from high-cristobalite, $[111]_c$, $[1\bar{1}0]_c$, $[11\bar{2}]_c$ and $[001]_c$ respectively. It is apparent that, although diminished in intensity, the diffuse scattering from low-cristoba-

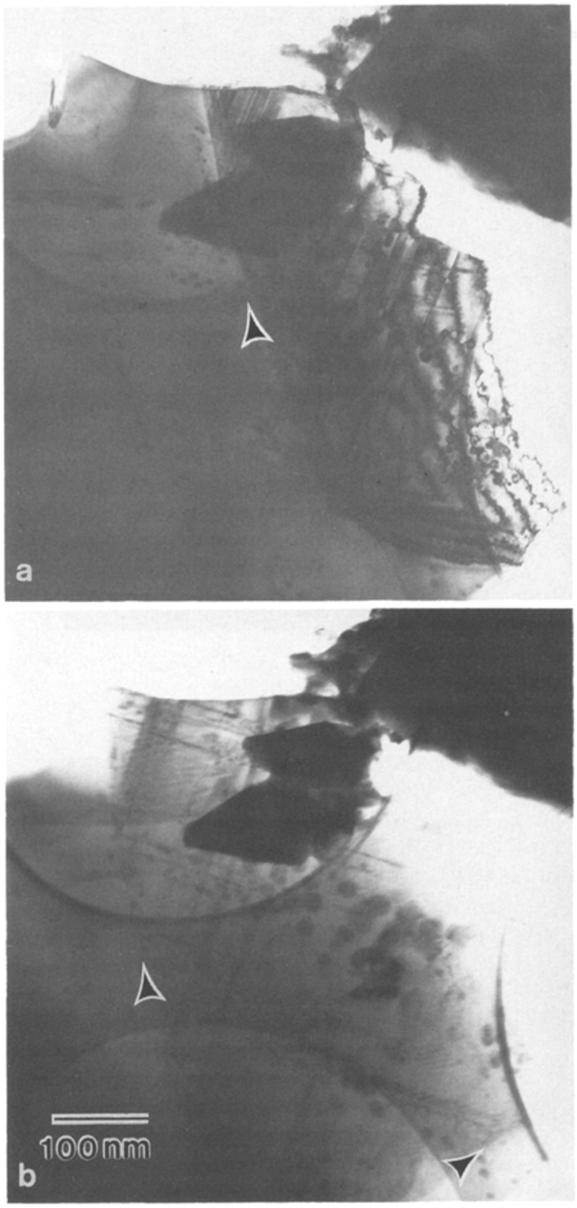

Fig. 7 a, b. Two low-magnification TEM bright-field images (**a**)–(**b**) of the same crystal of low-cristobalite in the same orientation after successive cyclings through the $\alpha\leftrightarrow\beta$ phase transition. Twin boundaries (*solid arrows*) are able to change both position and orientation, suggesting that there is no memory effect, and therefore, that impurities are not important

lite is similar in form to that from high-cristobalite. In particular, it is still localized in sheets perpendicular to what were the $<110>$ directions of high-cristobalite. It follows that the type of motion responsible for the diffuse intensity distribution in high-cristobalite must still occur in low-cristobalite. Nevertheless, there are significant differences apart from the general diminution of its intensity. Compare, for example, the diffuse intensity distributions present at the [111] zone axis of high-cristobalite with that found at the corresponding $[021]_t$ zone axis of low-cristobalite (see Fig. 4a, b). Of the six independent streak directions present in the high form only two are readily visible in the low form. When a diffraction pattern is taken at this zone axis from a region including this plus another tetragonal variant, however, a further two of the original six independent streak directions appear (see Fig. 5b). The freezing in of the $\mathbf{q} = <001>^*$ modulation, i.e., the choice of the tetragonal **c**-axis, clearly strongly affects the relative amplitudes of vibration of the 6 (originally equally likely) $<110>$-correlated tetrahedral rotations. There is, in the literature, much theoretical interest in predicting the variation of silicate framework geometry in response to temperature and pressure variations (see, for example, Pluth et al. 1985). The relatively large amplitude root-mean-square atomic displacements refined from neutron and X-ray diffraction studies of low-cristobalite hamper these investigations. Analysis of the characteristic diffuse intensity distributions present in both high- and low-cristobalite would seem to be the only way to take into account the time correlation between the thermal motion of adjacent atoms.

2. *Tetragonal Twinning*

Widely spaced (several μm) twin boundaries separating tetragonal twin variants are commonly observed. As reported by Christie et al. (1971), the composition planes are usually parallel to $\{112\}_t$ or $\{200\}_t \equiv \{101\}_c$ (see Fig. 5). Occasionally, however, composition planes $\{012\}_t \equiv \{112\}_c$, $\{011\}_t \equiv \{111\}_c$ and even curved composition planes have been observed (see Fig. 6). On warming through the $\alpha-\beta$ phase transition at ~265° C, these large scale twin boundaries disappeared. On cooling back into low-cristobalite below ~240° C, similar twin boundaries re-appeared but not in the same position or even necessarily the same orientation (see Fig. 7a, b). There is, therefore, no suggestion of memory effects caused by impurities.

3. *Characteristic Striations*

In addition to the large scale tetragonal twin boundaries, Figures 5 and 7 show the presence of fine scale (several hundred Å) defect structures within a single tetragonal twin variant. At certain zone axis orientations, it is possible to image these defect structures in the form of a fine scale pattern (~200–300 Å) of striations which represent the traces of 2 sets of intersecting planar boundaries (see Fig. 8a). The corresponding diffraction pattern (Fig. 8b), in addition to the more-or-less continuous diffuse streaks perpendicular to the $<110>_c$ directions, shows characteristic V-shaped diffuse streaks pointing along the $(2,0,1)_t^*$ and $(0,2,1)_t^*$ reciprocal lattice directions, i.e., $(2,\bar{2},1)_c^*$ and $(2,2,1)_c^*$, perpendicular to the planar boundaries of Figure 8a.

Christie et al. (1971) have reported a similar defect structure and interpreted it in terms of closely-spaced stacking faults parallel to $\{111\}_c$. The planar boundaries in Figure 8, however, are *not* $\{111\}_c$. Figure 9 demonstrates a possible resolution of this conflict. Again the characteristic pattern of edge-on planar boundaries is visible, but this time, they occur at a much more acute angle to each other (Fig. 9a). The corresponding diffraction pattern (Fig. 9b) again shows the characteristic V-shaped diffuse streaks – but this time pointing along $(1,0,2)_t^*$ and $(0,1,2)_t^*$ $(\equiv(1,\bar{1},2)_c^*$ and $(1,1,2)_c^*)$ for variant 1, i.e., the planar boundaries seem to be able to exist on either $\{2,0,1\}_t$ or $\{1,0,2\}_t$ planes. This, in turn, suggests that the planar boundaries may, in fact, be able to exist on any $\{1,0,l\}_t$

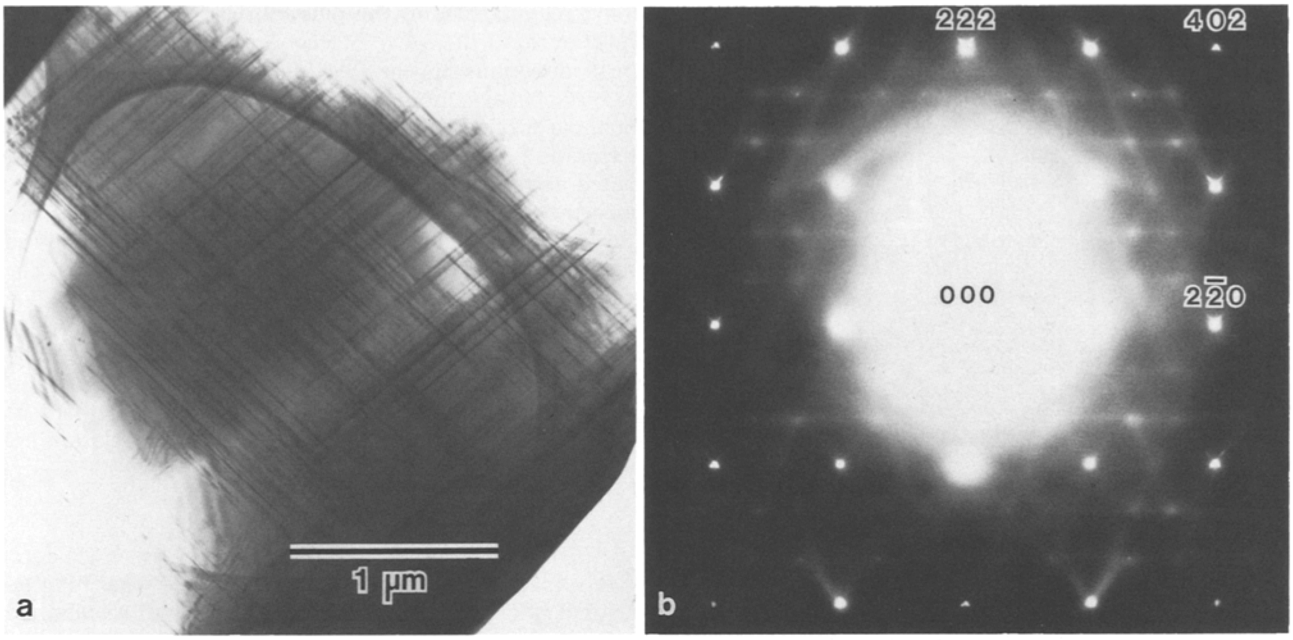

Fig. 8a, b. Low-magnification TEM bright-field image (**a**) and corresponding SADP (**b**) down the [11$\bar{2}$]$_t$ zone axis. Fine scale (200–300 Å) striations are visible in the image corresponding to streaking in the SADP along the $(2, 0, 1)_t^*$ and $(0, 2, 1)_t^*$ directions

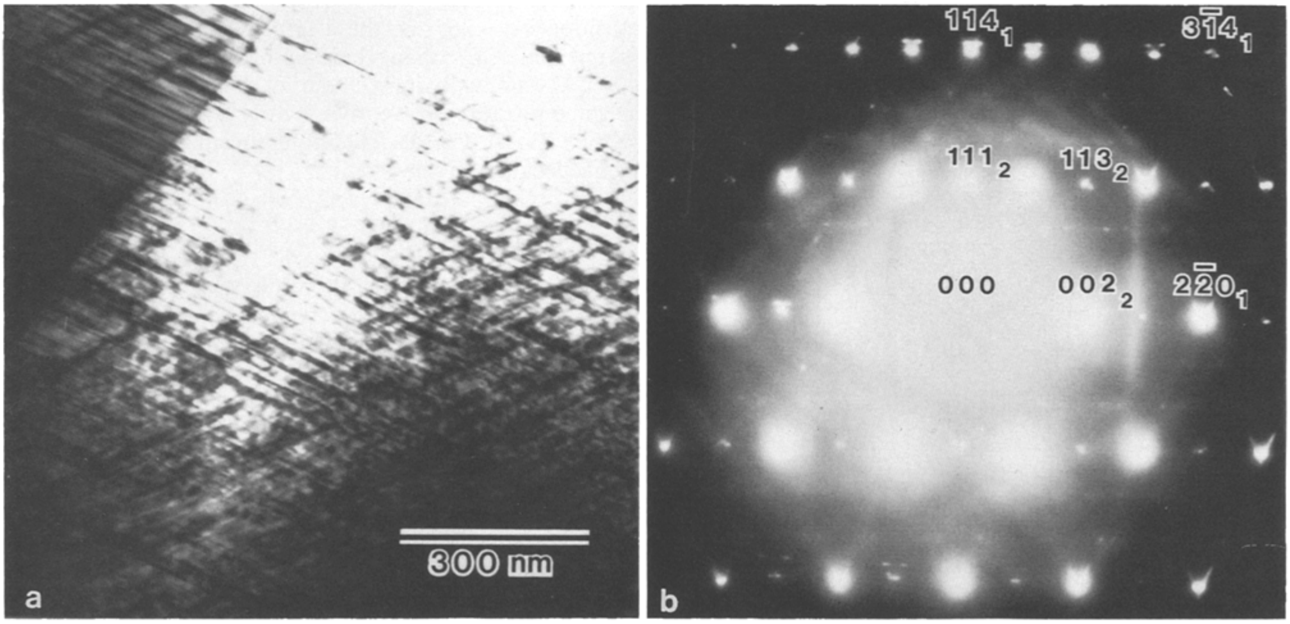

Fig. 9a, b. Low-magnification TEM bright-field image (**a**) and corresponding SADP (**b**) down the [22$\bar{1}$]$_t$ zone axis for variant 1. Fine scale striations are visible as for Figure 8a but occur along different directions. Streaking observed in the SADP is along the $(1, 0, 2)_t^*$ and $(0, 1, 2)_t^*$ directions

(and the equivalent $\{0, 1, l\}_t$) plane. The characteristic V-shaped diffuse streaks always point along $(1, 0, l)_t^*$ and $(0, 1, l)_t^*$ reciprocal lattice directions. Confirmation that the $(1, 0, l)_t$ planar boundaries can, in fact, vary is evident from the twisted planar boundary arrowed in Figure 10. This image is taken at the same orientation and from the same grain as that of Figure 8a, but after warming into the high-state and then returning to the low-state. Similarly to the large scale tetragonal twin boundaries, the fine scale defect structures show no memory effect. Given this variability in the planar boundary orientation, it is intriguing that only two sets of intersecting striations are ever visible in any one tetragonal variant.

In order to test the possibility that the boundaries represent simple displacement faults characterized by a shift vector **R**, satellite dark field images were taken using various operating reflections **g** and a zone axis orientation in the close vicinity of [11$\bar{2}$]$_t$. Systematic row conditions could always be easily obtained with only a small tilt away from [112]$_t$. Satellite dark field images were taken using operating reflections $\mathbf{g} = (1, \bar{1}, 0)_t^*$, $(3, 1, 2)_t^*$ $(0, 2, 1)_t^*$ and $(1, 1, 1)_t^*$. For

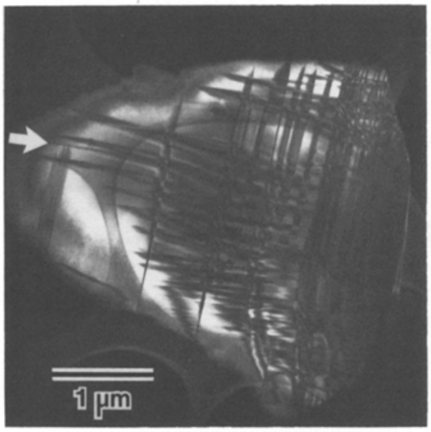

Fig. 10. Low-magnification TEM satellite dark-field image of the same crystal of low-cristobalite shown in Figure 8a but after cycling through the $\alpha \leftrightarrow \beta$ phase transition. The boundary (*arrowed*) is evidently twisted

Fig. 11. A higher magnification $\mathbf{g} = (1, \bar{1}, 0)_{\mathrm{f}}^{*}$ satellite dark field image as for Figure 8a showing in greater detail the complicated contrast variation

no operating reflection, however, could the boundaries be made to go out of contrast. This would seem to rule out the possibility of simple, low index displacement faults – in particular, the $1/2(\mathbf{a}+\mathbf{b})_c$ and $1/2(\mathbf{b}+\mathbf{c})_c$ origin shifts discussed earlier. This does not, however, rule out the possibility of shifts close to the latter but with a small irrational component due to strain (see, for example, Bursill and Hyde 1970).

Figure 11 shows a higher magnification $\mathbf{g} = (1, \bar{1}, 0)_{\mathrm{f}}^{*}$ satellite dark field image from a region of the same grain. There are some very complicated contrast variations, the interpretation of which is not at all clear to the present authors. A more detailed electron microscope study will therefore be needed to determine the exact nature of these boundaries and the structural reasons underlying their orientational flexibility.

Conclusion

Low-cristobalite exhibits a characteristic diffuse intensity distribution which, although much diminished in intensity, is undoubtedly closely related to that which exists in high-cristobalite. In addition, low-cristobalite exhibits a complex array of microstructural defects on both the fine (~200–300 Å) and the large (~several µm) scale. The exact nature of the boundaries involved and their relationship to high-cristobalite, however, requires further study.

Acknowledgements. This work has benefited greatly from extensive discussions with Professor Bruce G. Hyde. The technical assistance of Mr. Peter Barlow is also gratefully acknowledged.

References

Bradley CJ, Cracknell AP (1972) The mathematical theory of symmetry in solids. Clarendon Press, Oxford

Bursill LA, Hyde BG (1970) The displacement vectors of {132} and {101} faults in rutile. Proc R Soc Lond A320:147–160

Christie JM, Lally JS, Heuer AH, Fisher RM, Griggs DT, Radcliffe SV (1971) Proc Lunar Sci Conf 2nd. MIT Press 1:69–89

Hua GL, Welberry TR, Withers RL, Thompson JG (1988) An electron diffraction and lattice-dynamical study of the diffuse scattering in β-cristobalite, SiO_2. J Appl Crystallogr 21:458–465

International tables for crystallography, vol A (1983) Hahn T (ed) Reidel, Dordrecht Boston

O'Keeffe M, Hyde BG (1976) Cristobalites and topologically-related structures. Acta Crystallogr B32:2923–2936

Pluth JJ, Smith JV, Faber J Jr (1985) Crystal structure of low cristobalite at 10, 293, and 473 K: variation of framework geometry with temperature. J Appl Phys 57:1045–1049

Wyckoff RWG (1925) The crystal structure of the high-temperature form of cristobalite (SiO_2). Am J Sci 209:448–459

Received September 19, 1988